Structural and magnetic modifications of Cr-implanted Permalloy

J. Fassbender, J. von Borany, A. Mücklich, K. Potzger, and W. Möller
Institute of Ion Beam Physics and Materials Research, Forschungszentrum Rossendorf, P.O. Box 51 01 19, 01314 Dresden, Germany

J. McCord and L. Schultz
IFW Dresden, Institute for Metallic Materials, P.O. Box 270116, 01171 Dresden, Germany

R. Mattheis
Institute for Physical High Technology, P.O. Box 100 239, 07702 Jena, Germany
(Received 30 January 2006; revised manuscript received 6 April 2006; published 9 May 2006)

The static and dynamic magnetic properties, especially the magnetic damping behavior, have been investigated as a function of saturation magnetization in thin Permalloy films. Ion implantation doping with Cr in the percentage regime has been used to effectively reduce the Curie temperature and the saturation magnetization at room temperature. In order to understand the magnetic modifications the changes in stoichiometry but also the ion-induced structural changes have been addressed. As a function of fluence first an improvement of the (111) fiber texture, then a lattice expansion, and finally a partial amorphization of the interface near region of the Permalloy layer are found. The region of amorphization can be understood quantitatively by the concentration profiles as a function of depth in combination with irradiation-induced damage formation. The magnetic properties change correspondingly. For increasing Cr doping a drop in saturation magnetization and a decrease of the uniaxial magnetic anisotropy is observed. For a fluence of 0.8×10^{16} Cr/cm^2 ($\approx$4 at. %) the magnetic damping parameter α increases by a factor of more than 3. This strong increase is mainly caused by doping effects.

DOI: 10.1103/PhysRevB.73.184410 PACS number(s): 75.70.−i, 75.50.Cc, 61.72.Ww, 61.80.Jh

I. INTRODUCTION

The use of NiFeCr alloys as buffer layers has been demonstrated to be of crucial importance for the performance of high-density storage devices.[1–3] This is mainly due to the fact that a pronounced (111) texture of these sputtered Permalloy ($Ni_{81}Fe_{19}$) films with large grain sizes is required in order to optimize the magnetic properties. In addition the sheet resistance is altered, giving rise to better magnetoresistance characteristics. However, this behavior can best be achieved by using a buffer layer system which is close to the adjacent ferromagnetic film—i.e., Permalloy—but is nonetheless paramagnetic. One way to fulfill these requirements is the simultaneous deposition of Cr and $Ni_{81}Fe_{19}$ in order to reduce the Curie temperature of the forming film well below room temperature. Cr is a good candidate because it is particularly effective in lowering the Curie temperature in NiFe alloys, especially when the Ni content is high as in the case of Permalloy. From the bulk phase diagram it is well known that already about 8% Cr are sufficient to reduce the Curie temperature in Ni below room temperature.[4]

This potential for effectively reducing the Curie temperature and the saturation magnetization is employed to study the static and dynamic magnetic properties of Permalloy films as a function of saturation magnetization at room temperature. In the present study ion implantation is used for the doping. The major advantage of this technique over codeposition is that also doping in laterally confined areas is possible, giving rise to a pure magnetic patterning of simple ferromagnetic films without significantly affecting the surface topography.[5–9] In contrast to most investigations reported so far[5–8] the magnetic behavior can locally be altered between ferromagnetic and paramagnetic. The proof of principle has already been demonstrated by Folks *et al.*[9] However, these authors concentrated on the patterning potential at rather high ion fluences ($2–5\times10^{16}$ Cr/cm^2) for Permalloy films in the thickness range between 25 and 100 nm. Neither the structural modifications caused by the ion implantation process nor the change in magnetic anisotropy and damping behavior have been addressed. In a number of other investigations[10–12] it has also been demonstrated that solely the energy impact during ion irradiation can also give rise to changes in magnetism. Therefore it is essential to investigate both the structural and magnetic modifications caused by the ion implantation.

Special effort is put on the dynamic magnetic characterization and the determination of the magnetic relaxation rate λ_{LL} which enters the Landau-Lifshitz torque equation

$$\frac{1}{\gamma}\frac{\partial\vec{M}}{\partial t} = -[\vec{M}\times\vec{H}_{eff}] - \frac{\lambda_{LL}}{\gamma M_S^2}(\vec{M}\times[\vec{M}\times\vec{H}_{eff}]), \quad (1)$$

which is commonly used for the description of the magnetization precession.[13,14] In addition to the gyromagnetic ratio γ and the saturation magnetization M_S the uniaxial magnetic anisotropy K_u enters via the effective field $\vec{H}_{eff}=\vec{H}_{appl}+\vec{H}_k$, with $\vec{H}_{appl}$ the applied magnetic field and $\vec{H}_k=(2K_u/M_S)\hat{e}_x$ the uniaxial anisotropy field (easy axis parallel to $\hat{e}_x$). The more often used phenomenological damping constant α can be determined using $\lambda_{LL}=\alpha\gamma(4\pi M_s)$. Scientific interest in damping phenomena[15] has been considerably renewed in recent years because for high-speed switching devices control of the magnetization trajectory is crucial.[16,17] However, the design of material parameters for optimization of the mag-

netic damping behavior is still in its infancy.[18–20]

The paper is organized as follows. In Sec. II the experimental details are described, covering aspects of sample preparation, ion implantation, structural characterization by means of x-ray diffraction, cross-section transmission electron microscopy and Rutherford backscattering, and magnetic characterization by means of magneto-optic Kerr effect and pulsed inductive microwave magnetometry. In Sec. III the results are presented and discussed. This section is divided into three subsections addressing (A) structural characterization, (B) characterization of the implantation profile and the corresponding interfacial mixing, and (C) magnetic characterization. Finally, the paper is summarized in Sec. IV.

II. EXPERIMENTAL DETAILS

Permalloy samples have been prepared on top of a Ta buffer layer by sequential large-area magnetron sputter deposition at room temperature on a 6-in. SiO_2/Si substrate. The nominal stacking sequence is $(20\ \text{nm}\ Ni_{81}Fe_{19})/(5\ \text{nm}\ Ta)/SiO_2/Si$ substrate. During deposition an in-plane magnetic field of 50 Oe has been applied in order to set the uniaxial magnetic anisotropy direction. The anisotropy field is determined to 5 Oe which corresponds to an anisotropy constant of $2.15\times10^3\ \text{erg/cm}^3$. In order to reduce the number of interfaces and thus decrease the potential intermixing during ion irradiation no cap layer has been added. After deposition the structure was protected from corrosion by a thin photoresist layer which was removed prior to ion implantation in an ethanol bath. Then the samples have been implanted at room temperature with 30-keV Cr ions in the fluence regime up to $2\times10^{16}\ \text{ions/cm}^2$. The ion current density has been limited to $0.6\ \mu\text{A/cm}^2$ in order to avoid sample heating. According to SRIM simulations[21] the mean projected range of the Cr ions is $R_p=11.7$ nm (straggling: 6.6 nm); i.e., the Cr ions are implanted close to the midplane of the Permalloy film. More detailed simulations of the implantation profile have been performed using the TRIDYN code.[22] These will be presented in Sec. III B.

The structural characterization of the as-deposited and ion-implanted samples has been performed by x-ray diffraction (XRD) on a commercial Bruker-AXS D8 diffractometer using the Cu $K\alpha$ line. In addition cross-sectional transmission electron microscopy (XTEM) using a Philips CM300 microscope was carried out for selected samples to collect information concerning the crystallographic structure and the film morphology from bright-field imaging and electron diffraction. Rutherford backscattering spectrometry (RBS) using 1.7-MeV He ions has been applied to investigate the elemental redistribution and the sputtering effect during ion irradiation. In order to increase the depth resolution, an incident angle of 70° has been used. The static magnetic characterization has been performed predominantly by longitudinal magneto-optic Kerr effect (MOKE) analysis. Helmholtz coils provide the applied magnetic field to avoid remanence effects and thus allow for an accurate determination of small magnetic fields. A diode laser with $\lambda=405$ nm wavelength has been chosen in order to optimize the signal-to-noise ratio by maximizing the achievable Kerr rotation in the optical wavelength regime. The polarization rotation has been determined by two photodiodes sensing the two mutually orthogonal polarization directions in an optical bridge configuration. Since a modification of the Kerr rotation magnitude is not a direct measure of the magnetization, the contributions of magneto-optical effects have to be considered. Therefore inductive (*B-H*-looper) measurements have been performed on selected samples using a SHB Instruments system. From these measurements the maximum error is estimated to +10% of the initial magnetization; i.e., MOKE analysis yields larger values than inductive measurements.[12]

For the dynamic magnetic characterization and the determination of the saturation magnetization a pulsed inductive microwave magnetometer (PIMM) is used.[23] For this, the sample is placed face down on top of a 0.5-mm-wide coplanar microwave transmission line. A magnetic field step excitation ($\approx$2 Oe) is provided by launching a 100-ps-rise-time, 23-ns-long current pulse through the waveguide into a high-bandwidth (13-GHz) sampling oscilloscope. If a magnetization precession is excited, it induces an inductive signal in the waveguide which is superpositioned on the initial current pulse. In order to extract this tiny signal the background is measured in an external field sufficient to saturate the magnetization along the direction perpendicular to the waveguide center conductor direction. In this configuration no magnetization precession is excited since the magnetization and the magnetic field pulse are collinear. Then an external field is applied along the waveguide direction in order to maximize the cross product between $\vec{M}$ and $\vec{H}_{appl}$ and thereby excite a magnetization precession. From this measured signal the background is subtracted which allows us to determine the inductive signal of the precessing magnetization alone. This method is the time-domain equivalent to a ferromagnetic resonance measurement with a pulse instead of a continuous wave excitation. The frequency and relaxation rate is determined by fitting an exponentially decaying damped sine function to the data. A variation of the applied magnetic field allows in addition determination of the dynamic anisotropy and the saturation magnetization.

III. RESULTS AND DISCUSSION

A. Structural characterization

The XRD scans measured in symmetrical Bragg-Brentano geometry confirm the strong (111) texture of the Permalloy films since only the (111) and (222) reflections are obtained in the diffraction pattern. Figure 1(a) shows the Permalloy (111) reflection for the as-deposited film and a series of different Cr implantation fluences as indicated in the figure. The detailed courses of the (111) peak intensity and the lattice constant as a function of Cr fluence are plotted in Fig. 1(b). For an implantation fluence of $0.2\times10^{16}\ \text{ions/cm}^2$ the peak intensity increases by about a factor of 2 compared to the as-deposited sample and distinct Laue fringes appear at the low-angle side of the peak. The peak position itself remains unaffected. The mean grain size according to Scherrer's formula is 14 nm—i.e., slightly smaller than the Permalloy film thickness of 17.5 nm, which has been determined by trans-

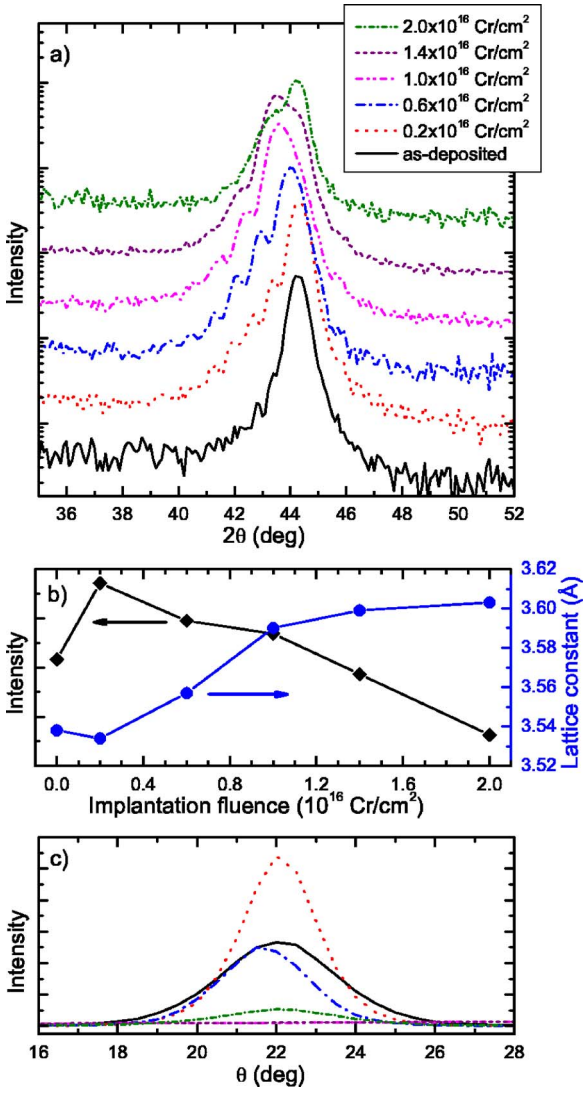

FIG. 1. (Color online) (a) X-ray diffraction pattern of the Permalloy (111) reflex in Bragg-Brentano geometry for the as-deposited sample and a series of different Cr implantation fluences as indicated in the figure. (b) Integrated (111) peak intensity (diamonds) and determined lattice constant (circles) as a function of Cr implantation fluence. (c) Rocking curves for the as-deposited and the Cr-implanted films [see (a)].

mission electron microscopy (TEM). This difference reflects the critical thickness which is necessary to form a well-oriented (111) texture in the Permalloy film on the Ta buffer. Both the increased peak intensity and the Laue fringes confirm the improvement of the film quality—i.e., a decrease of the mosaicity and a homogenization of the crystalline thickness. This is correlated with a significant reduction of the peak width obtained in the rocking curve (θ scan for fixed 2θ) as presented in Fig. 1(c). SRIM simulations indicate that even for a fluence of 2×10^{15} ions/cm^2 each atom in the Permalloy film is displaced several times during ion irradiation. Although the mean grain size does not change, the ion-irradiation-induced reordering leads to an enhancement of the (111) fiber texture.[24] Upon further implantation the intensity of the (111) peak decreases continuously and the peak position shifts to smaller scattering angles; i.e., the perpendicular lattice spacing increases according to the Cr incorporation.[25] For a fluence of 1×10^{16} ions/cm^2 the (111) lattice distance has increased by approximately 1.7%. Ion implantation fluences above 1×10^{16} ions/cm^2 lead first to a double-peak structure. For higher fluences one of the peaks is shifted back towards the original peak position. This behavior is attributed to significant changes in the film composition due to ion beam mixing. As shown in detail later, the ion irradiation leads to an incorporation of Ta in the Permalloy film and to a decrease of the Ni concentration as a function of depth. The Ta mixing is related to an amorphization of the Permalloy which lowers the obtained diffraction intensity if the Ta content in the films exceeds a certain level.[26,27] In addition the Ni depletion with depth is compensated by the Cr incorporation. It is supposed that the Ni positions are substituted by Cr in the lattice in accordance with the Fe-Ni-Cr ternary phase diagram.[28]

In order to support the interpretation of a partial amorphization of the Permalloy film for the highest ion fluence, cross-sectional TEM has been performed. Figure 2(a) shows a bright-field image of the layer system prior to ion implantation. The SiO_2 substrate, the 5-nm Ta buffer layer, and the 17.5-nm $Ni_{81}Fe_{19}$ film can easily be distinguished due to the mass contrast and well-defined interfaces. The polycrystalline Ta film exhibits the tetragonal β-Ta phase as derived from the lattice plane distance of single grains. The Permalloy film exhibits a columnar structure throughout the whole film thickness. From the high-resolution image in Fig. 2(a) the (111) lattice planes are found to be nearly parallel to the surface and the mean lattice distance of 0.207 nm is close to the tabulated value of Permalloy [$d(111)=0.205$ nm].[29] The corresponding selected-area diffraction (SAD) pattern is shown in Fig. 2(b) confirming the strong (111) texture of the Permalloy film. The situation has changed significantly after high-fluence (2×10^{16} ions/cm^2) Cr implantation [see Fig. 2(c)]. Due to sputtering which accompanies the ion implantation, the total film thickness is reduced by approximately 4 nm. Furthermore, as a result of the ion beam mixing, the Ta buffer layer and the Permalloy film cannot be resolved any longer from the contrast in the micrograph. Adjacent to the SiO_2 interface, at least half of the metallic film is transformed to an amorphous state. Since no amorphous NiFeCr alloy has been reported so far, it had been generally expected that Cr implantation would not cause an amorphization of the Permalloy film. Thus, the amorphization is attributed to the mixed Ta content in the film. The remaining still $\langle111\rangle$-textured crystallites are located at the film surface.

B. Effects of implantation profile and ion beam mixing

For a quantitative interpretation of the observed structural modifications, it is helpful to address the phenomena during ion irradiation—i.e., the formation of the implantation profile and the effect of ion beam mixing. For this purpose, TRIDYN simulations have been performed and compared to RBS investigations. For the TRIDYN simulations[22] the sample has been modeled by a 20-nm $Ni_{81}Fe_{19}$ layer on top of a 5-nm Ta layer on a Si substrate [see Fig. 3(a)]. Si has been used in-

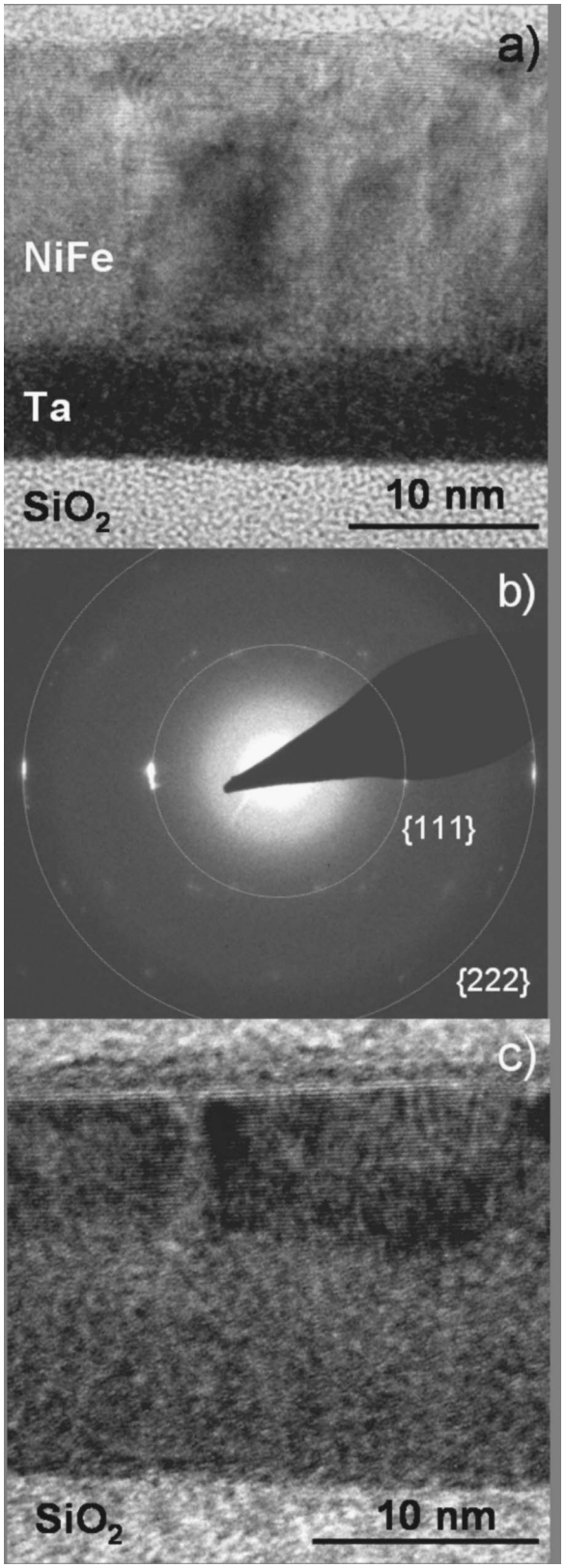

FIG. 2. (a) High-resolution cross-sectional TEM image of the as-deposited sample. The individual layers are labeled. (b) Selected-area diffraction pattern from a region of 1 μm diameter of the as-deposited sample. (c) High-resolution image of a sample after Cr ion implantation with a fluence of 2×10^{16} ions/cm^2. Crystalline regions are only observed close to the sample surface.

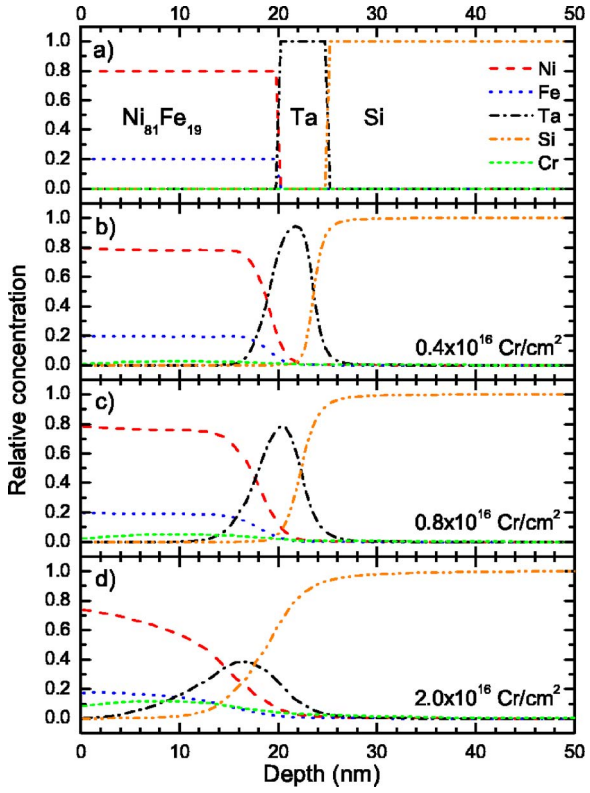

FIG. 3. (Color online) TRIDYN simulations of the relative concentrations of the individual elements as a function of sample depth before implantation (a) and for implantation fluences of 0.4×10^{16} ions/cm^2 (b), 0.8×10^{16} ions/cm^2 (c), and 2×10^{16} ions/cm^2 (d).

stead of SiO_2 due to the limited number of elements available in the present TRIDYN code. For the surface binding energies the enthalpies of sublimation for Ni, Fe, and Cr have been inserted.[30] Abrupt interfaces between the respective layers are assumed. The Cr implantation energy is 30 keV; the implantation direction is normal to the surface. Figures 3(b)–3(d) show the resulting compositional profiles for the implantation fluences of 0.4, 0.8, and 2×10^{16} ions/cm^2, respectively. Already for the smallest fluence a broadening of the Ta profile is observed which increases at increasing implantation fluence. Accordingly the interfaces between the individual layers become blurred. From the initially 20 nm of Permalloy only about 15 nm are left after an implantation fluence of 2×10^{16} ions/cm^2 [see Fig. 3(d)]. However, the actual interface position cannot be determined accurately due to the broad profiles. Instead, TRIDYN yields a surface recession of 6.8 nm at that fluence. Compared to the cross-section TEM image [Fig. 2(c)] the sputter yield is therefore overestimated by the computer simulations. In the top 15 nm an average Cr concentration of 10 at. % is reached. In addition, in a depth regime between 11.5 and 20.5 nm, which is approximately half of the residual metallic film thickness, the Ta concentration reaches values above 21 at. %. This Ta concentration is actually the critical concentration of Ta in Ni above which irradiation induced amorphization takes place.[26] The critical concentration of Ta in Permalloy is probably even lower.[27] Thus the

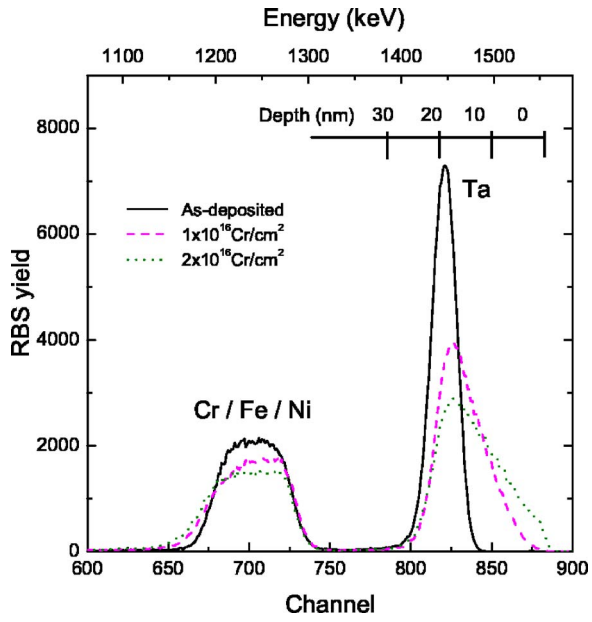

FIG. 4. (Color online) RBS spectra sections of the as-deposited film and for different Cr implantation fluences with respect to the Ta and mixed Cr-Fe-Ni signals. The depth scale for the Ta distribution is based on an atomic concentration in the film of 9×10^{22} cm^{-3} (bulk Permalloy value).

observed amorphization of the metallic film close to the SiO_2 interface can be attributed to interfacial mixing between the Ta buffer layer and the Cr-implanted Permalloy layer. Although from the cross-section TEM image [Fig. 2(c)] an even larger amorphized region is determined, the agreement between TRIDYN simulations, the calculated critical concentration for ion-induced amorphization,[26] and the actual TEM image is quite stunning. Especially it has to be noted that no data are available for the critical Ta concentration in the ternary NiFeCr system which easily might explain this slight discrepancy between theory and experiment.

In order to experimentally determine compositional implantation profiles, RBS measurements have been performed. The corresponding spectra for the as-deposited film and after Cr ion implantation at fluences of 1 and 2×10^{16} ions/cm^2 are shown in Fig. 4. The irradiation-induced redistribution of the Ta towards the surface is obvious. After an implantation of 2×10^{16} ions/cm^2 Ta is distributed throughout the whole Permalloy film and half of the film contains a Ta content >20 at. %. This result agrees with the TRIDYN calculations and the amorphized Permalloy region obtained by TEM. Due to the small difference in their masses, Cr, Ni, and Fe cannot be separated with respect to their depth profiles. However, from the reduction in the integrated areal density (see Fig. 4) the sputter loss can be estimated. The total Ni and Fe losses are estimated to 2.1×10^{16} atoms/cm^2 and 3.6×10^{16} atoms/cm^2 after an Cr implantation of 1 and 2×10^{16} ions/cm^2, respectively, which corresponds to a sputtering of 2.3 and 4 nm, respectively, in agreement with the TEM result.

C. Magnetic characterization

As mentioned above it is well known that alloying Permalloy with Cr leads to a reduction in Curie temperature and

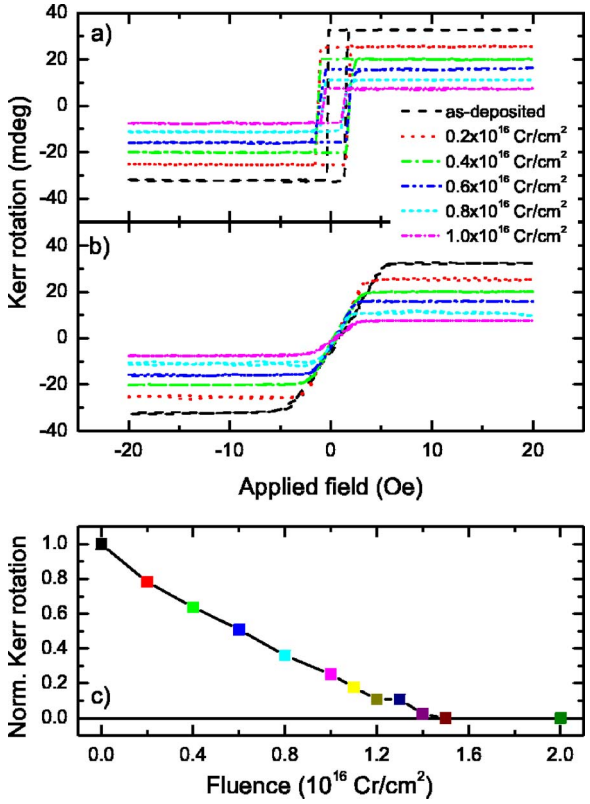

FIG. 5. (Color online) Easy-axis (a) and hard-axis (b) in-plane magnetization reversal curves of the layer system determined by longitudinal magneto-optic Keff effect analysis. The magnetization reversal curves are shown for the as-deposited and a series of Cr-implanted samples. The Cr implantation fluence is indicated in the figure. In (c) the normalized Kerr rotation magnitude—i.e., the total Kerr rotation of the implanted sample divided by that of the as-deposited one—is shown as a function of implantation fluence. Additional inductive measurements on selected samples have shown that the normalized Kerr rotation magnitude is proportional to the relative magnetization of the film (Ref. 12) and overestimate the magnetization by at most 10% of the initial saturation magnetization.

in saturation magnetization. The reduction in magnetization is now investigated by means of magneto-optic Kerr effect analysis. The in-plane easy- and hard-axis magnetization reversal curves are shown in Figs. 5(a) and 5(b), respectively. The different curves correspond to the as-deposited and Cr-ion-implanted samples. With increasing ion fluence the Kerr rotation magnitude is progressively decreased. This behavior is shown normalized to the initial Kerr rotation magnitude in Fig. 5(c). For an implantation fluence of 1.5×10^{16} ions/cm^2 which corresponds to a doping concentration of about 8 at. % Cr throughout the Permalloy film, the magnetization vanishes. For the implanted samples a slight increase of the coercivity due to additional pinning sites created by the implantation process is found [see Fig. 5(a)]. The saturation field for the hard-axis loops and thus the uniaxial anisotropy are reduced with increasing Cr fluence. In order to investigate the magnetic anisotropy in more detail, a full angular dependence of the magnetization reversal behavior is performed. The corresponding magnetic remanence data of

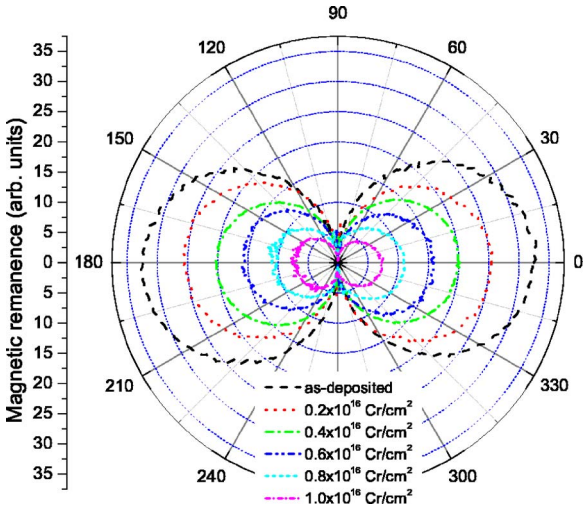

FIG. 6. (Color online) Angular dependence of the magnetic remanence for the same samples as in Fig. 5. The twofold symmetry and thus the uniaxial magnetic anisotropy are clearly observed for all samples.

the individual hysteresis loops are shown in Fig. 6. For all samples investigated a clear twofold symmetry is observed which reflects the uniaxial anisotropy of these samples. Since the magnetic field during ion implantation has been applied along the initial easy magnetization direction, the ion implantation leaves the symmetry of the anisotropy unchanged.

Next we turn to the investigation of the magnetization dynamics. For this purpose PIMM measurements have been performed for a series of applied magnetic fields ranging from 0 to 20 Oe. For an applied field of 10 Oe the transient inductive signal is shown in Fig. 7(a) for the same samples as characterized in Fig. 5. Larger fluences than 0.8

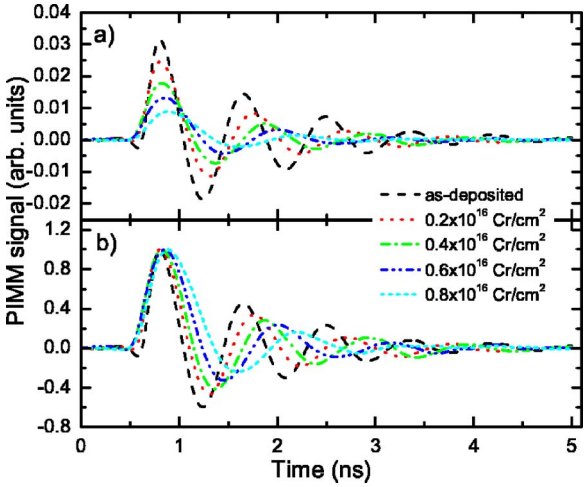

FIG. 7. (Color online) (a) Time-dependent inductive signal of the magnetization traces in response to a 100-ps rise time step pulse for the same samples as shown in Fig. 5. The coplanar waveguide center conductor exhibits a width of 0.5 mm, enabling a pulse field of 2 Oe. The applied static field is 10 Oe. (b) The same data as in (a) but normalized to the first maximum. This representation allows a better qualitative comparison of the magnetic relaxation rates by inspecting the exponential decay of the oscillating signals.

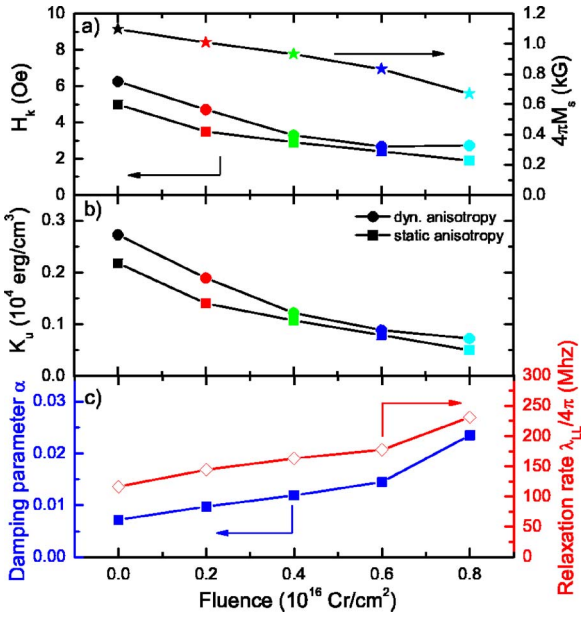

FIG. 8. (Color online) (a) Static (squares) and dynamic (circles) anisotropy field $\mathbf{H}_k$ as a function of Cr implantation fluence. In addition the saturation magnetization determined by PIMM is shown for the as-deposited and Cr-implanted samples. (b) Resulting effective static (squares) and dynamic (circles) uniaxial anisotropy constant K_u as a function of Cr fluence. (c) Magnetic relaxation rate $\lambda_{LL}/4\pi$ (diamonds) and magnetic damping parameter α (squares) as a function of Cr fluence.

$\times 10^{16}$ ions/cm^2 could not be investigated due to the insufficient inductive signal arising from the precessing magnetization with a strongly reduced magnetization value. In order to achieve an easier comparison between as-deposited and ion-implanted samples in Fig. 7(b) the same data as in Fig. 7(a) are presented in a normalized fashion; i.e., the first oscillation maximum has been set to 1 by multiplying the original data by a constant factor for each implantation fluence. From Fig. 7(b) two features can already be observed qualitatively: (i) the precession frequency ω is reduced and (ii) the relaxation rate λ_{LL} given by the decaying envelope is increased as a function of ion fluence. In order to determine these parameters quantitatively each transient inductive signal was fitted to an exponentially decaying sinusoidal function of the form

$$\Phi(t) = \beta \sin(\omega t + \phi)\exp(-t\lambda_{LL}/2), \tag{2}$$

with $\Phi(t)$ the time-dependent PIMM signal, β and ϕ the amplitude and phase of the oscillation, and t the time. Using Kittel's formula[31]

$$\omega^2 = \gamma^2 H_{eff}(H_{eff} + 4\pi M_S), \tag{3}$$

with $\vec{H}_{eff} = \vec{H}_{appl} + \vec{H}_k$ in the limit $H_{eff} \ll 4\pi M_S$, the dynamic H_k can be determined by a linear extrapolation of $\omega^2(H_{appl}) \to 0$. The intersection with the abscissa yields $-H_k$. The slope of the linear fit yields $4\pi M_s$. The dynamic anisotropy fields H_k and saturation magnetizations $4\pi M_s$ determined by this method are shown in Fig. 8(a) as a function of Cr implantation fluence. The static anisotropy field, deter-

mined from the hard-axis magnetization reversal loops [see Fig. 5(b)], are shown in Fig. 8(a) for comparison. The static and dynamic anisotropy fields agree within 1 Oe. The slight discrepancy between both has also been observed for other material systems (see, e.g., Ref. 32). The corresponding uniaxial anisotropy constants given by $K_u = \frac{1}{2} M_S H_k$ are shown in Fig. 8(b). For a fluence of 0.8×10^{16} ions/cm^2 H_k is reduced by a factor of 2.6 and the saturation magnetization by a factor of 1.6. The reduction of the uniaxial anisotropy constant combines both effects.

The extracted relaxation rates λ_{LL} for applied fields $H_{appl} \geq 10$ Oe for each sample have been averaged and plotted as function of ion fluence in Fig. 8(c). For a fluence of 0.8×10^{16} ions/cm^2 an increase by a factor of 2 with respect to the pure Permalloy value is found. Due to the drop in saturation magnetization, which enters the phenomenological damping constant α, the increase in α is by a factor of 3.2 [see Fig. 8(c)]. For an ion fluence of 0.8×10^{16} ions/cm^2 which corresponds to an approximate doping concentration of 4 at. % the change in magnetic damping constant ($\alpha = 0.024$) with respect to the pure Permalloy sample ($\alpha = 0.008$) is $\Delta\alpha = 0.016$. Rantschler *et al.*[20] observed a value of $\Delta\alpha = 1.109 \times 10^{-3}$/at. %—i.e., $\Delta\alpha = 0.0044$, which is about a factor of 3 smaller than the values observed here. The discrepancy in these values is attributed to the different sample preparation techniques—i.e., cosputter deposition versus ion implantation. It has already been shown that the magnetic damping parameter can depend sensitively on the microstructure.[33] As already discussed in Sec. III B the broadening of the Ta buffer layer profile has to be considered which gives rise to an additional unintentional doping of an interface near region of the Permalloy layer. The magnitude of this effect for an ion fluence of 0.8×10^{16} ions/cm^2 can be estimated as follows. Considering the TRIDYN simulation presented in Fig. 3(c) a residual magnetic film thickness of 20 nm is assumed. Furthermore, in the top 15 nm (bottom 5 nm) a homogeneous doping with 4 at. % Cr (40 at. % Ta) is assumed. Although these assumptions are very crude, they should give an estimate for the overall magnetic damping to be expected considering doping effects only. In the case of Ta doping Rantschler *et al.*[20] report a value of $\Delta\alpha = 0.892 \times 10^{-3}$/at. %. This gives rise to a damping value of $\alpha_{Cr} = 0.0124$ and $\alpha_{Ta} = 0.0404$ for the Cr- and Ta-doped regions, respectively. Song *et al.*[34] reported that the total magnetic damping of a bilayer consisting of two individual layers with different magnetic damping constants can be determined as the thickness-weighted average of the individual damping constants. Applying this procedure to the above-specified model bilayer a magnetic damping constant of $\alpha = 0.0194$ would be expected originating from doping effects only. This number is only 20% smaller than the experimentally determined value of $\alpha = 0.024$. The remaining discrepancy is attributed to the following effects: (i) The crystallinity of the ion-implanted samples is strongly affected by the implantation process itself. This gives rise to a modified saturation magnetization with respect to cosputtered samples. Furthermore, due to the different incorporation of the doping atom into the lattice, the arising lattice strain might lead to additional relaxation channels enhancing the overall magnetic damping. (ii) Dephasing effects which correspond to an inhomogeneous broadening in ferromagnetic resonance. These effects have been determined separately and excluded from the ferromagnetic resonance data of Rantschler *et al.*[20] and cannot be accounted for in our time-domain measurements. In view of the large differences in the structural properties of ion-implanted and cosputtered samples the arising difference in the magnetic damping parameter of 20% is not surprising.

IV. SUMMARY AND CONCLUSION

Ion implantation doping of thin Permalloy films has been performed in order to modify the saturation magnetization, the magnetic anisotropy, and the magnetic damping behavior. In order to understand the modifications of the magnetic properties the accompanying changes in the crystallographic structure due to the ion implantation process have to be addressed. It is found that upon Cr implantation first the lattice expands and for higher fluences amorphous as well as crystalline phases are observed. The amorphization of the interface near region is explained by a combination of irradiation induced Ta profile broadening, which leads to a mixture of Ta with Permalloy, and the subsequent amorphization of the Ta-Permalloy alloy due to irradiation. A strong reduction of saturation magnetization and also a reduction of magnetic anisotropy as a function of Cr ion fluence are observed. The magnetic damping is strongly increased upon ion implantation. This increase cannot be explained by doping effects only. In addition radiation-induced damage and a change of the crystalline structure are to be considered. To further clarify the effects of radiation damage and crystallinity on the magnetic damping properties of Permalloy films noble-gas irradiation experiments will be performed. In addition, in order to circumvent the unintentional Ta doping a different layer system employing a thick paramagnetic NiFeCr interlayer between the Permalloy and Ta buffer layers will be used in further experiments.

ACKNOWLEDGMENTS

The authors like to thank J. O. Rantschler and R. D. McMichael for sharing their results on magnetic damping constants of doped Permalloy films prior to publication. The technical support of I. Winkler, who is responsible for the ion implantation, is gratefully acknowledged.

[1] W.-Y. Lee and D. Mauri, U.S. Patent 5,731,936 (1998).
[2] W.-Y. Lee, M. F. Toney, P. Tameerug, E. Allen, and D. Mauri, J. Appl. Phys. **87**, 6992 (2000).
[3] J. R. Childress, M. J. Carey, R. J. Wilson, N. Smith, C. Tsang, M. K. Ho, K. Karey, S. A. MacDonald, L. M. Ingall, and B. A. Gurney, IEEE Trans. Magn. **37**, 1745 (2001).
[4] R. M. Bozorth, *Ferromagnetism* (IEEE Press and Wiley, Hoboken, NJ, 2003).
[5] W. M. Kaminsky, G. A. C. Jones, N. K. Patel, W. E. Booij, M. G. Blamire, S. M. Gardiner, Y. B. Xu, and J. A. C. Bland, Appl. Phys. Lett. **78**, 1589 (2001).
[6] D. Ozkaya, R. M. Langford, W. L. Chan, and A. K. Petford-Long, J. Appl. Phys. **91**, 9937 (2002).
[7] D. McGrouther and J. N. Chapman, Appl. Phys. Lett. **87**, 022507 (2005).
[8] J. McCord, T. Gemming, L. Schultz, J. Fassbender, M. O. Liedke, M. Frommberger, and E. Quandt, Appl. Phys. Lett. **86**, 162502 (2005).
[9] L. Folks, R. E. Fontana, B. A. Gurney, J. R. Childress, S. Maat, J. A. Katine, J. E. E. Baglin, and A. J. Kellock, J. Phys. D **36**, 2601 (2003).
[10] S. I. Woods, S. Ingvarsson, J. R. Kirtley, H. F. Hamann, and R. H. Koch, Appl. Phys. Lett. **81**, 1267 (2002).
[11] R. Gupta, K.-H. Han, K. P. Lieb, G. A. Müller, P. Schaaf, and K. Zhang, J. Appl. Phys. **97**, 073911 (2005).
[12] J. Fassbender and J. McCord (unpublished).
[13] M. Bauer, J. Fassbender, B. Hillebrands, and R. L. Stamps, Phys. Rev. B **61**, 3410 (2000).
[14] J. Miltat, G. Albuquerque, and A. Thiaville, in *Spin Dynamics in Confined Magnetic Structures I*, edited by B. Hillebrands and K. Ounadjela, Topics in Applied Physics Vol. 83 (Springer-Verlag, Berlin, 2002).
[15] B. Heinrich, in *Ultrathin Magnetic Structures III*, edited by J. A. C. Bland and B. Heinrich (Springer-Verlag, Berlin, 2005), p. 143.
[16] T. Gerrits, H. A. M. van den Berg, J. Hohlfeld, L. Bär, and T. Rasing, Nature (London) **418**, 509 (2002).
[17] S. E. Russek, R. D. McMichael, M. J. Donahue, and S. Kaka, in *Spin Dynamics in Confined Magnetic Structures II*, edited by B. Hillebrands and K. Ounadjela, Topics in Applied Physics Vol. 87 (Springer-Verlag, Berlin, 2003), p. 93.
[18] S. G. Reidy, L. Cheng, and W. E. Bailey, Appl. Phys. Lett. **82**, 1254 (2003).
[19] S. Ingvarsson, G. Xiao, S. S. P. Parkin, and R. H. Koch, Appl. Phys. Lett. **85**, 4995 (2004).
[20] J. O. Rantschler and R. D. McMichael (private communication); J. O. Rantschler, D. Pulugurtha, L. M. Connors, A. Chen, A. Castillo, A. Shapiro, W. F. Egelhoff, Jr., R. D. McMichael, and B. B. Maranville (unpublished).
[21] J. F. Ziegler, J. P. Biersack, and U. Littmark, computer code SRIM 2003, *The Stopping and Range of Ions in Solids* (Pergamon, New York, 1985).
[22] W. Möller, W. Eckstein, and J. P. Biersack, Comput. Phys. Commun. **51**, 355 (1988). The TRIDYN code is available at www.fz-rossendorf.de
[23] T. J. Silva, C. S. Lee, T. M. Crawford, and C. T. Rogers, J. Appl. Phys. **85**, 7849 (1999).
[24] S. J. Park, D. P. Norton, and V. Selvamanickam, Appl. Phys. Lett. **87**, 031907 (2005).
[25] E. D. Specht, A. Rar, G. M. Pharr, E. P. George, P. Zschack, H. Hong, and J. Ilavsky, J. Mater. Res. **18**, 2522 (2003).
[26] B. X. Liu, W. S. Lai, and Q. Zhang, Mater. Sci. Eng., B **29**, 1 (2000).
[27] J. Fassbender, A. Mücklich, K. Potzger, and W. Möller, Nuclear Instruments and Methods in Physics Research B (to be published).
[28] E. D. Specht, P. D. Rack, A. Rar, G. M. Pharr, E. P. George, J. D. Fowlkes, H. Hong, and E. Karapetrova, Thin Solid Films **493**, 307 (2005).
[29] Powder-Diffraction-File: 38-0419, International Centre for Diffraction Data.
[30] For the enthalpies used see Gmelin Data Base, MDL Information Systems GmbH, Germany.
[31] C. Kittel, *Introduction to Solid State Physics*, 7th ed. (Wiley, Hoboken, NJ, 2005).
[32] R. Lopusnik, J. P. Nibarger, T. J. Silva, and Z. Celinski, Appl. Phys. Lett. **83**, 96 (2003).
[33] W. Bailey, P. Kabos, F. Mancoff, and S. Russek, IEEE Trans. Magn. **37**, 1749 (2001).
[34] H. Song, L. Cheng, and W. E. Bailey, J. Appl. Phys. **95**, 6592 (2004).